Three-dimensional controlled-source electromagnetic and magnetotelluric joint inversion

Michael Commer and Gregory A. Newman

Lawrence Berkeley National Laboratory, 1 Cyclotron Road, Berkeley, CA 94720

SUMMARY

The growing use of the controlled-source electromagnetic method (CSEM) and magnetotellurics (MT) for exploration applications has been driving the development of data acquisition technologies, and three-dimensional (3D) modeling and imaging techniques. However, targeting increasingly complex geological environments also further enhances the problems inherent in large-scale inversion, such as non uniqueness and resolution issues. In this paper, we report on two techniques to mitigate these problems. We use 3D joint CSEM and MT inversion to improve the model resolution. To avoid the suppression of the resolution capacities of one data type, and thus to balance the use of inherent, and ideally complementary information content, different data reweighting schemes are proposed. Further, a hybrid model parametrization approach is presented, where traditional cell-based model parameters are used simultaneously within a parametric inversion. The idea is to limit the nonuniqueness problem, typical for 3D imaging problems, in order to allow for a more focusing inversion. The methods are demonstrated using synthetic data generated from models with a strong practical relevance.

1 INTRODUCTION

Large-scale inverse problems are usually under-determined, meaning that there are more unknowns, typically in the form of highly digitized model meshes, than data. This adds to the problem that errors are associated with every geophysical datum. The resulting issue is referred to as the problem of non-uniqueness of inverse solutions. To mitigate this problem and to improve the resolution in an inversion, it is common to take advantage of complementary natures of different geophysical data sets. In electromagnetic problems, magnetotelluric (MT) data usually provides the conductivity information on a more gross scale, while controlled source electromagnetic methods (CSEM) have a better ability of illuminating rather subtle targets, particularly thin resistors. MT data have been successfully combined with time-domain CSEM data to invert for one-dimensionally layered models (Hui-Ping et al. 1996; Meju 1996; Rovetta et al. 2008). With CSEM data responding stronger to thin resistive targets, the combination with MT data has a strong relevance for providing a less ambiguous interpretation of data measured over hydrocarbon prospects. Mackie et al. (2007) report a proof of concept showing the improved resolution by combining marine CSEM and MT synthetic data for mapping thin resistors.

Even with improved resolution capabilities, the solutions of 3D large-scale cell-based (or pixel-based) inversions with finely sampled models usually remain non-unique. Several strategies have been reported to limit the ambiguities for reconstructed targets and its conductivities. For cell-based problems, model-smoothing constraints are commonly applied, limiting the solutions to a class of geologically more meaningful ones, i.e. avoiding conductivity variations that are unphysical. A different approach is to actually address the under-determinacy by casting the problem into a parametric problem. Common parametric solutions to EM inverse problems (including CSEM and MT) allow the determination of boundaries between regions of contrasting conductivities, while avoiding superfluous detail (Smith et al. 1999; de Groot-Hedlin & Constable 2004; Commer et al. 2006; Zhang et al. 2007). A model parametrization can for example be based on interfaces known from seismic reflection data. The obvious drawback of such methods is the necessity of sufficient background information in order to define a suitable model parametrization. Here, we propose a hybrid approach, overlaying a cell-based inversion over a particular area of interest with a paramet-

ric inversion over a regional scale. This combines the advantages of cell-based and structure-based model parameters.

In this work, we present three joint inversion examples using synthetic CSEM and MT data. All examples have been carefully designed in order to provide realistic examples as well as to address important aspects to be considered when jointly inverting EM data. One aspect of paramount importance is to weight a data type in order to fully exert its characteristic resolution strength within the inversion process without bestriding the influence of the other type. The first example features the hybrid model parametrization. Moreover, it demonstrates the flexibility of our inverse solution to be applied to data collected from surface surveys. Different ways of estimating properly balanced data weights are discussed within the following two studies, where marine hydrocarbon prospecting scenarios are simulated.

2 METHODOLOGY

Our inversion algorithm's underlying finite-difference (FD) forward modeling algorithm for EM field simulation solves a modified form of the vector Helmholtz equation for scattered or total electric fields. The theoretical principles and numerical implementation for parallel computers are outlined in detail by Alumbaugh et al. (1996). Details about the inversion algorithm can be found in the works of Newman & Alumbaugh (1997; 2000), and Commer & Newman (2008) . We use a non-linear conjugate gradient (NLCG) approach to minimize a general objective function Φ,

$$\Phi = \Phi_d + \Phi_m = \frac{1}{2}\sum_i \left\{[\mathbf{D}_i(\mathbf{d}_i^o - \mathbf{d}_i^p)]^H[\mathbf{D}_i(\mathbf{d}_i^o - \mathbf{d}_i^p)]\right\} + \frac{1}{2}\lambda(\mathbf{W}\mathbf{m})^H(\mathbf{W}\mathbf{m}), \quad (1)$$

where H denotes the Hermitian operator. The summation term describes the data constituent, Φ_d, of the objective function and the summation (i) occurs over the number of different data types in the data input. Each data term consists of the vectors of observed and predicted data, $\mathbf{d}_i^o$ and $\mathbf{d}_i^p$. The diagonal weighting matrix $\mathbf{D}_i$ defines the degree of influence of the corresponding data on the inversion process. Using the underlying FD forward modeling algorithm, the predicted data are initially computed from a starting model, which is iteratively refined during the course of the inversion. The second term applies a smoothing matrix, $\mathbf{W}$, to the vector of model parameters, $\mathbf{m}$.

In order to minimize model curvature in all three spatial dimensions, we usually apply a finite-difference approximation to the Laplacian operator (∇^2). Minimizing the model roughness term Φ_m acts as a stabilizer to avoid geologically unrealistic images. The regularization parameter λ balances the influence of Φ_d and Φ_m on the image solution. We refer the interested reader to the work of Newman & Boggs (2004) for details on its selection. For the CSEM-MT joint inverse problem, the gradient of the total objective function shall be written as

$$\nabla\Phi = \nabla\Phi_{CSEM} + \nabla\Phi_{MT} + \nabla\Phi_m. \tag{2}$$

2.1 A hybrid model parametrization approach

In general, parametrization is a way of defining the parameters of some model that are salient to the qualitative question and quantities to be estimated from that model. In 3D imaging, a common way is to use the elements comprising a digitized FD or finite-element mesh of parameters, which is also referred to as cell-based (or pixel-based) approach. The simplicity of this approach comes at the expense of a high degree of solution non-uniqueness, owing to the under-determinacy of the inverse problem that has a much higher number of parameters than actual observations. Several strategies have been reported to limit the ambiguities for reconstructed targets and its conductivities. For cell-based problems, model-smoothing constraints are among the most common strategies to limit the solutions to a class of geologically more meaningful ones, thus avoiding too much spatial variation in the material parameters.

A different approach is to address the under-determinacy by casting the EM inverse problem into a parametric problem. The definition of geometric shapes in parametric solutions requires a priori information and assumptions. In the context of EM inversions, the geological a priori knowledge is often provided by seismic reflection data, where one assumes that horizons of different acoustic impedances also exhibit electrical conductivity contrasts (Hoversten et al. 2000). The two-dimensional sharp boundary inversion (SBI) approach by Smith et al. (1999) is parametrized to accommodate sharp contrasts in resistivity across layer interfaces. The model unknowns thus become boundaries between layers and its conductivities assigned to the boundary nodes. While showing benefit, especially for verification of images obtained from other methods (Hoversten

et al. 2000; Commer et al. 2006), parametric methods usually come at the expense of strongly affecting the resulting models.

Here, it is proposed to keep the high degree of freedom provided by pixel-based inversions within a focusing area of interest, while using a simple parametric model for the regional conductivity model. In principle, the regional model parameters are constructed by pooling together the corresponding grid cells of the underlying model grid defining the inversion domain. Consider the gradient vector of a cell-based model, with M unknown cell parameters,

$$\nabla\Phi = (g_1, g_2, ..., g_M)^T$$

We predefine fixed structures by combining the gradient vector components of the cells within the structure volume, specifically

$$G_m = \frac{1}{M_m}\Sigma_{i=1}^{M_m} g_i,$$

where M_m defines the number of grid cells contained within a structure parameter's volume. Dividing the combined gradient component by M_m ensures a balance between differently sized parameters of this kind. The electrical conductivity is constant within this volume and is an unknown parameter to be optimized. Structures of arbitrary shapes can be constructed in this way. In this work, we do not consider variable structure boundaries, but experiment with a hybrid inversion scheme, using both cell-based and parametric unknowns at the same time. The "hybrid" gradient vector is then composed of M^p parametric components, also referred to as structure parameters in the following, and M^c cell-based components,

$$\nabla\Phi = (G_1, G_2, ..., G_{M^p}, g_1, g_2, ..., g_{M^c})^{\mathrm{T}}$$

The idea is to keep the high degree of freedom, provided by cell parameters, within a certain volume of interest, while seeking to greatly reduce the total number of unknowns outside of this volume by a "coarser" parametrization, so $M^p + M^c \ll M$. Below, we present an example where such a hybrid parametrization helps to illuminate a deep region of interest, which cannot be properly imaged by using a purely cell-based method over the whole model.

2.2 Balancing data weights

For a number of N_i data points, assigned to a given data type i, the total data constituent of the objective function in eq. 1 can also be written as

$$\Phi_d = \frac{1}{2}\Sigma_i \Sigma_{n=1}^{N_i} \Delta_n \Delta_n^*. \tag{3}$$

The complex data difference term Δ_n, with * denoting its complex conjugate, is constructed from the in-phase (Re) and quadrature (Im) parts of the data points (here i =imaginary unit),

$$\Delta_n = Re(d_n^o - d_n^p)Re(w_n) + iIm(d_n^o - d_n^p)Im(w_n), \tag{4}$$

where d_n^o represents an observed datum, and d_n^p is predicted through forward modeling. The data weights, w_n, are the components of the weighting matrix $\mathbf{D}_i$ of eq. (1), and are usually based upon the inverse of the standard deviations of the measurements.

In a typical joint inversion of CSEM and MT data for exploration purposes, particularly in marine surveys with a moving CSEM transmitter, it can be expected that the number of CSEM data points greatly exceeds the number of MT data points. Assuming that both data types have similar noise levels, it will be shown in examples below that the more numerous CSEM data can cause the influence of the MT data on the imaging outcome to become insignificant. As a remedy, similar to the model regularization parameter λ, one can consider additional trade-off parameters between the data constituents in eq (1). However, in this work we do not employ further trade-off parameters, but impose a properly balanced data influence directly through the data weights. For the mentioned marine case, this would involve enhancing the MT data against the CSEM data. It may require a number of imaging experiments until a set of weights $\mathbf{D}_i$ can be deemed as the most consistent obtained with the available time and computing resources. In this work, we experiment with a cooling approach as suggested for selecting a proper model regularization parameter (Newman & Hoversten 2000).

As an alternative, two methods for directly estimating data re-weighting factors shall also be proposed. The first scheme of approaching an equal balance simply considers the number of data points each data method contributes. Two data sets, 1 and 2 (CSEM and MT, respectively), shall

contain a number of data points given by N_1 and N_2, where $N_1 > N_2$. Data set 2 is then up-weighted by applying a factor f_w,

$$\tilde{w}_n = w_n f_w; \qquad f_w = \sqrt{\frac{N_1}{N_2}}, \tag{5}$$

to its data weights, where the square root stems from the fact that Φ_d depends quadratically on w_n. This scheme assumes that one has a high confidence in the original standard deviations of the measurements. Furthermore, such a method is likely to achieve a balanced data influence only when both data methods are characterized by similar intrinsic sensitivities. The latter vanishes with less overlap in model resolution capacities between two data sets, which may call for additional up-weighting of the MT data.

The second data re-weighting scheme uses norms of the gradients, considering only the data constituents in eq (2). Here, the up-weighting factor f_w for data set 2 is computed from

$$f_w = \sqrt{\frac{||\nabla\Phi_{CSEM}||}{||\nabla\Phi_{MT}||}}. \tag{6}$$

Computing the gradient norms from the initial (starting) model, the method has the advantage of providing a fast estimate of the intrinsic data sensitivities, which incorporates both the quantity and resolution capacity in a joint data set.

2.3 Grid design

In the following, a variety of examples is presented, with a wide range of survey geometries and signal frequencies. Each synthetic data set involves two sets of FD simulation grids, here also called computing grids. The first is for the actual data generation and is a set of fine (oversampled) grids, in order to have some degree of independence from the forward modeling process during the actual inversion of the synthetic data. The inversion employs coarser meshes, where the spatial extension and the grid sampling rate are adapted specifically to the survey geometries and signal frequencies, respectively. In general, lower frequencies allow for a coarser sampling. The concepts for optimizing the computing grid design are outlined in detail in an earlier work (Commer & Newman 2008). In this preceding work, we refer to the mesh defining the model parametrization, and including the imaging domain, as the modeling grid. The modeling grid sampling is chosen

according to the desired degree of resolution in the parametrization. The proper material averaging scheme for mapping between modeling grids and computing grids are also outlined in detail in the mentioned work.

3 SYNTHETIC DATA INVERSION STUDIES

In the following, three synthetic data inversion studies are presented. The examples are chosen such that each one covers different aspects of practical relevance for joint inversion problems. Only in-line electric field components shall be considered for the CSEM data. The fields are generated from horizontal electric dipole (HED) transmitters with finite lengths. For the MT stations, we always consider point dipoles and invert only the two off-diagonal impedance tensor elements Z_{xy} and Z_{yx}. In accordance with an earlier MT inversion study (Newman et al. 2002), the diagonal components, Z_{xx} and Z_{yy}, exhibit a rather noisy behavior for the MT frequency band used in the studies presented here. Hence, these data are omitted, as they were not found to improve the shown imaging results. The data errors are computed from the data amplitudes and are 3 % for CSEM and 1 % for MT, both with a Gaussian distribution. For the shown inversion attempts, unless mentioned otherwise, the relative data misfit decrease ($RDMD$),

$$RDMD(\%) = \left| \frac{\Phi_d(n) - \Phi_d(n-1)}{\Phi_d(n-1)} \right| * 100$$

between successive inversion iterations, $n-1$ and n, shall be chosen as a stopping criteria. More precisely, over a course of a predefined and always enforced maximum number of iterations, the solution is extracted from the inversion iteration where the $RDMD$ drops below a given threshold for the last time.

3.1 CO_2 sequestration monitoring study

The first study presented demonstrates the advantages of a proper model parametrization, while at the same time it shall also serve as a practical example for a monitoring scenario using surface CSEM and MT measurements together.

The sequestration of carbon dioxide (CO_2) is considered as a means to mitigate the environ-

mental effects due to carbon emissions from the burning of fossil fuels. Starting in the late 1990s, the research in this area has grown into a multi-faceted effort with geophysical monitoring methods playing a crucial role. Therefore, accurate modeling and imaging techniques are required for a complete understanding of the long-term performance issues at large industrial storage sites. To provide a high level of confidence that the injected gas will remain sequestered permanently, an emphasis is on the geologic response in the intermediate zone between the injection point and the surface area. Most geophysical monitoring activities addressing this task thus far have involved seismic methods, see for example recent reports by Lumley et al. (2008) or White (2008). While other methods include the cross-borehole EM technique (Kirkendall & Roberts 2004), the authors are not aware of any pilot studies involving surface EM techniques. The questions to be answered by the following study is to what degree a resistive plume can be imaged by combining surface CSEM and MT measurements. Moreover, can the movement of a CO_2 plume be monitored ?

Fig. 1 introduces the model of an underground gas reservoir at depth overlaid with the positions of surface-based CSEM and MT field stations. The station setup (a) comprises 15 MT stations spread over an area of $4 \times 4\,\mathrm{km}^2$. Each station measures 9 MT frequencies, ranging logarithmically from 0.1 to 10 Hz. HED CSEM transmitters of length 100 m are located at each end of the centrally located receiver profile. The profile contains 38 in-line electric field detector points, excited by three CSEM frequencies, 0.25, 0.75, and 1.25 Hz. Because of a relatively balanced amount of data points, 228 CSEM data points and 270 MT data points, no additional data weighting is employed in this example.

The principal assumption for this case study is that major features of the geology surrounding the target location of interest, i.e. the injection area, are known a priori. Much a priori information can be expected to be available. Designated sequestration sites are either former oil or natural gas production areas with an already good understanding of the underlying geology. In undeveloped fields, preceding site characterization and feasibility studies can be expected to provide a structural knowledge base. The background is chosen to be a horizontally layered geology with 7 layers of contrasting electrical conductivities, underlying the target region of interest (Fig. 1b). Here, it shall be assumed that the injection of gas at a depth of $z = 1500$ m causes a conductivity drop to

0.005 S/m within a volume of 0.8 km^3, which could be explained by a volume increase and thus a pressure drop, vaporizing the CO_2 to a gaseous state. Such a large response is considered in this example, since only surface measurements are used.

The imaging volume is shown by Fig. 1c, where the green lines depict the underlying cell-based model (parametrization) grid, and the white lines outline the shapes of the horizontal layer structure parameters. The parametric unknowns are 20 layers with a thickness of 100 m, and the base layer below $z = 2000$ m. Note that the underlying computational FD grid, not shown here, is different to the model grid, since we design optimal grids adapted specifically to the CSEM/MT signal frequencies and layouts. The model grid has a sampling interval of 100 m within the cell-based imaging volume, depicted by the white rectangle. This volume represents the injection area and extends from -2500 to 2500 m horizontally and $z = 1200 - 2000$ m, which amounts to 16807 FD model grid cells. Note that each layer interrupted by the cell-based imaging volume still forms one structure parameter. The total number of unknowns for the hybrid parametrization is $M^p + M^c = 16828$, compared to $M = 108000$ for the completely cell-based inversion.

A homogeneous half-space with $\sigma = 0.1$ S/m and a resistive layer ($\sigma = 10^{-4}$ S/m) for the air space is used as starting model. One-dimensional comparisons showed that this conductivity contrast (1000:1) provides for sufficient solution accuracy. It shall be mentioned as a side note that the conductivity contrasts in a model affect the iterative Krylov solver convergence of the forward solution. To benefit from the fact that lower contrasts generally improve the convergence, we seek to minimize the conductivity contrast between the air and the earth. More details on this Krylov solver convergence issue, there in the context of modeling topography, can also be found in the work of Commer et al. (2006) and references therein.

We have carried out both standalone CSEM and MT inversions as well as joint inversions using a pixel-based parametrization over the whole model domain, which involves 108000 cell parameters. However, the target's depth and the sparsity of the data account for the failure to properly resolve the region of interest. Starting from the half-space model, the inversions end in a local minimum without significant changes to the target region. The image of a pixel-based joint inversion is shown in Fig. 2. Here, the true layered background (Fig. 1b) was used as starting

model. The result demonstrates the non-uniqueness problem. Significant conductivity changes only occur in the region close to the surface. While adequate gradient depth-weighting schemes can be used to enhance the resolution at greater depths, this shall not be further pursued in this work.

The first two inversion results using the hybrid parametrization are shown in Fig. 3. These are standalone CSEM and MT inversions and demonstrate the strengths of either method. The CSEM data can resolve the resistive injection volume depicted by the white rectangle. However, the layered background conductivities approach the true case only within the upper 1000 m. On the other hand, the MT inversion resolves the background to a better overall degree, while the data is not sensitive to the thin resistor. As a stopping criteria, we used a value $RDMD = 0.5$ %, which required 75 iterations for both results. This means that subsequent iterations did not achieve a higher relative misfit decrease over a maximum of 100 iterations.

The following Fig. 4 shows two joint inversion results. First, we inverted for a centrally located resistor (a). Below (b) is the result for a reservoir which is shifted by 1000 m to the left of its original x-axis position and 200 m upwards, without change along the y axis. The joint inversions show a clear improvement by combining the resolution capabilities of both methods. Compared to the standalone CSEM inversion, there is a much better agreement with the true resistivity of the target region. Furthermore, the result comes much closer to the true layered background, especially in the region above the reservoir. While the image of the resistor remains rather diffusive, and does not show the precise vertical location, a very small shift to the left can be observed in the lower figure.

The major conclusion to be drawn from this study is that the hybrid model parametrization is essential in illuminating the subtle target region. A purely cell-based inversion is not able to indicate the deep target due to a too sparse data coverage. Second, joint imaging may prove beneficial for EM time-lapse monitoring of sequestration sites. Not only does one seek to track conductivity changes due to a moving plume, but also changes in the background conductivity, which can be expected over seasonal time periods.

3.2 Marine prospecting study 1

The search for hydrocarbons now extends to highly complex and subtle offshore geological environments. An important exploration problem to demonstrate the advantages of joint conductivity inversion of CSEM and MT data is the imaging of oil bearing horizons in the presence of sub salt structures. The geometries of the reservoirs and salt structures are exceedingly difficult to map without recourse to 3D imaging. Such structures are encountered in the Gulf of Mexico, where seismic imaging beneath salt can be a formidable task. For oil bearing horizons above salt, the situation is better, but we will show that such structures can be identified much better under a joint imaging framework.

In Fig. 5 the survey setup on the sea bottom is plotted together with a projection of the reservoir at a depth of 1 km to the plotting plane. The inversion data set consists of 143 MT stations spread over a 25×25 km^2 grid. Each of the two impedance tensor elements Z_{xy} and Z_{yx} is measured for 13 MT frequencies, ranging (logarithmically) from $5 \cdot 10^{-4} - 0.125$ Hz. The grid of CSEM detectors is a sub grid of the MT station grid, with 63 locations comprising an area of 20×15 km^2. It is common to treat marine CSEM data in a reciprocal way, owing to a continuously moving transmitter along the sail lines of the vessel. Hence the actual receivers become computational transmitters, or sources, marked as CSEM stations in Fig. 5. With two CSEM frequencies, 0.25 and 0.75 Hz, for each source, we simulate a total of 126 sources oriented along the x-axis and with a length of 200 m. A total of 6468 in-line receivers, with a length of 100 m, are evenly spread over the lines marked as CSEM sail lines, which in reality would correspond to the lines of the moving transmitter. These lines are 50 m above the sea floor. Counting in-phase and quadrature components of the complex data, the total number of data points is $N_{CSEM} = 12936$ and $N_{MT} = 7436$.

Again, we want to compare the greatly improved image resulting from jointly inverting all data to the standalone inversion results. Figs 6 and 7 show the imaged volume as vertical xz-slices and horizontal xy-slices, respectively (same color scale as in Fig. 5). The original model (a) is based on an earlier sub-salt MT imaging study of the Mahogany prospect in the Gulf of Mexico (Newman et al. 2002). The marine model, with a sea water ($\varrho = 0.33\ \Omega \cdot \mathrm{m}$) column of 1 km,

features several interconnected salt bodies reaching a depth of over 6 km. The resistivity of these bodies, embedded into a 0.5 $\Omega \cdot \mathrm{m}$ background, averages 100 $\Omega \cdot \mathrm{m}$. Further, a hypothetical resistive ($\varrho = 50\ \Omega \cdot \mathrm{m}$) hydrocarbon reservoir with a thickness of 250 m is included at 1 km below the sea floor.

The image results of the separate CSEM and MT inversions (b and c in Figs 6 and 7) again show the different degrees of resolution achieved by either method. While the oil bearing horizon is clearly indicated by the CSEM image, yet without a clear delineation of the true shape, the MT data is only sensitive to the large salt bodies; however the MT image shows salt body conductivities which are generally above the true values. A great improvement is achieved by the joint inversion (d), both in terms of a delineation of the reservoir and salt bodies, as well as in reproducing the true conductivities. Note also that the depth of the salt bodies is reproduced to a fairly good degree.

For this study, we carried out a cooling approach to zero in on a balanced influence between the CSEM and MT data, such that both the shallow and deep model features are reproduced satisfactorily. In addition to image quality, a judging factor was also solution convergence. Starting with the original data weights, a too dominant CSEM data influence could be observed, resulting in an image similar to the standalone CSEM inversion. An optimal MT data re-weighting factor was found to be $f_w = 10$. As an experiment, a much larger factor ($f_w = 100$) was also tried, giving too much weight to the MT data and thus producing an image close to the MT standalone inversion result.

The image improvement also reflects in the much smaller data fitting errors, shown as error bars along the MT-stations and CSEM receiver profiles in Fig. 8. These errors were calculated using eqs (3) and (4) and further averaging over the respective number of data points at each detector location. Note that, for a comparison of the MT data fits, the MT errors of Fig. 8b are calculated with the same weights (enhanced by a factor of $f_w = 10$) as used for the joint calculation. Consequently the errors appear to be by a factor of 100 larger than the ones produced by the original errors. Using the original MT data weights, the MT standalone inversion result produces averaged errors with values below one at each station position. In addition to a smoother error variation across the survey area, it is also observed that the most significant error decrease in the joint in-

version result happens above the region with a larger subsurface concentration of the salt bodies ($y > 2.5$ km).

3.3 Marine prospecting study 2

The previous examples have shown that MT and CSEM data offer complementary information on subsurface electrical conductivity and it is therefore reasonable to combine both types of data in the imaging process in order to provide the most consistent view of the subsurface. So far, we have combined the data in a simultaneous way, and keep referring to this as joint inversion. However, it shall be pointed out that interpreting different data types can also involve the successive inversions of different data types. Often, each type of image is then analyzed independently and then overlaid to investigate its relationship with the other data type. In the following, we also experiment with a sequential approach, where the image produced from one data type feeds the starting model of the other data type. Specifically, it will be investigated whether the foregoing standalone MT inversion improves the image of the regional conductivity background, compared to a (simultaneous) joint inversion.

The example's layout, shown in Fig. 9a, is another marine prospecting study using the synthetic data from a single profile. The profile contains 7 CSEM source positions with a HED length of 50 m. Again, in a real-world scenario, these are the detector locations. The locations coincide with the MT stations. Further, we have three CSEM frequencies (Hz): 0.25, 0.5, and 1.25; 78 CSEM point-dipole receivers for each source at 50 m above the seafloor ($z = 0$); five MT frequencies (Hz): 0.01, 0.018, 0.032, 0.056, 0.1. The model for synthetic data creation comprises a 1 km deep sea column and a regional layered background with non-horizontal sine-shaped horizons which are invariant along the y-axis. Embedded at a depth from $z = 0.8 - 1$ km is a 0.01 S/m resistive reservoir, with a maximum (bottom side) size of 1 km along x and a strike of 1.65 km along y.

We choose a rather ideal horizontally layered starting model with the true layer conductivities (Fig. 9b), since the focus of this study shall only be to investigate to what degree both the reservoir body and the true layer interfaces are reproduced with different methods. Also, we use as stopping criteria a higher value, $RDMD = 3\%$, for the MT (standalone) inversion, since its only purpose

is to produce a starting model to launch a CSEM inversion. To compare all other results to each other, only the CSEM data is considered for the threshold of $RDMD = 0.5\%$. Both the standalone CSEM and MT inversions (Figs 9c,d) achieve a relatively good delineation of the upper layer interface. The CSEM image indicates the reservoir, yet with a few unrealistic anomalies away from the reservoir, around $x \pm 2.5$ km. In contrast, the MT image does not resolve the thin resistive reservoir, however achieves a slightly better delineation of the lower layer boundary.

Because of a relatively large ratio, $\frac{N_{CSEM}}{N_{MT}} = 23.4$, in the amount of the two data types, the (simultaneous) joint inversion result in Fig. 10a), produced with the original synthetic data weights, has a similar outcome as the standalone CSEM inversion. Clearly the beneficial MT resolution properties observed in the previous result are now suppressed. Therefore, in the next attempt (Fig. 10b), the model from the MT inversion is taken as starting model for a subsequent CSEM inversion, running for 30 more iterations after which the stopping criteria is met. The result clearly shows much better delineation of the background beds, together with a sharper image of the reservoir. Still, there is some inexactness in the vertical reservoir geometry. To assess the performance of this sequential approach, both data re-weighting schemes, eqs (5) and (6), are employed for the joint inversion results shown in Figs 10c,d, respectively. The corresponding factors applied to the MT data weights are $f_w = 4.8$ and $f_w = 8.2$. Both schemes enhance the MT data influence sufficiently such that the background model does not show the artifacts mentioned above produced by the CSEM inversion. In comparison, weighting scheme 1 produces a slightly closer match to the true reservoir conductivity.

In conclusion, estimating proper data re-weighting factors either through the ratios of the data amounts or the initial data gradient norms enhances the intrinsic resolution capacities of the MT data adequately. Comparing all four joint inversion results, the sequential approach is achieved at the lowest computational effort. While it provides a closer match to the low reservoir conductivity, the simultaneous joint inversion results reproduce the reservoir size slightly better.

4 CONCLUSIONS

We have presented a number of CSEM-MT joint imaging results of practical relevance with different aspects to be considered when combining different EM data types. An important finding is that a good understanding of the intrinsic resolution capacities of the different data types is essential in order to take full advantage of the information contained within each. Carrying out several standalone, sequential, and simultaneous inversion attempts may be necessary to gain such understanding, until a final image can be trusted. To produce maximally consistent images through joint inversions, all examples have shown the great importance of a proper data weighting.

The CO_2 sequestration study showed that, in addition to the improved resolution provided by the combined data, a more constrained model parametrization is also essential in order to extract the desired information about a subtle target at depth from surface measurements. It is anticipated that the sequestration monitoring efforts will routinely involve cross-borehole measurements, either seismic and/or EM. Hence, the next step would involve a joint inversion of both borehole and surface data. We believe that this has the potential to greatly improve the delineation of a CO_2 plume. Also, changes in the peripheral regions of the injection area can be tracked at the same time. If undiscovered, such changes may otherwise lead to false assumptions about plume geometries. The presented hybrid model parametrization can be imagined for a number of time-lapse imaging scenarios, especially at monitoring sites, where the background geology is usually known to a high degree.

The great power of combining marine MT and CSEM data for offshore hydrocarbon mapping has become clear in the two marine studies. In the first example, the MT data illuminated deep salt structures, which produced a much clearer rendering of the hydrocarbon bearing horizon in the combined data inversion. Likewise, the CSEM data helped to produce a sharper image of the salt than obtained from inverting the MT data alone. In view of the good delineation of the target structures, one can imagine the tremendous potential when overlaying or even jointly inverting with seismic data. The second marine study demonstrated some computational benefit of inverting different data types sequentially. Using the data containing the more regional information first, can produce a much closer starting model for a subsequent more focusing image of a subtle target.

This approach may serve as an alternative way when uncertainty exists about the proper weighting of different data types.

5 ACKNOWLEDGMENTS

This work was carried out at Lawrence Berkeley National Laboratory, with base funding provided by the ExxonMobil Corporation and the United States Department of Energy, Office of Basic Energy Sciences, under contract DE-AC02-05CH11231.

REFERENCES

Alumbaugh, D. L., Newman, G. A., Prevost, L. & Shadid J. N., 1996. Three-dimensional wideband electromagnetic modeling on massively parallel computers, *Radio Science*, **31**, 1-24.

Commer, M., Helwig, S. L., Hördt, A., Scholl, C. & Tezkan, B., 2006. New results on the resistivity structure of Merapi Volcano (Indonesia), derived from three-dimensional restricted inversion of long-offset transient electromagnetic data, *Geophys. J. Int.*, **167**, 1172-1187.

Commer, M. & Newman, G. A., 2008. New advances in three-dimensional controlled-source electromagnetic inversion, *Geophys. J. Int.*, **172** 513-535.

de Groot-Hedlin, C. & Constable, S., 2004. Inversion of magnetotelluric data for 2D structure with sharp resistivity contrasts, *Geophysics*, **69**, 78-86.

Hoversten, G. M., Constable, S. C. & Morrison, H. F., 2000. Marine magnetotellurics for base-of-salt mapping: Gulf of Mexico field test at the Gemini structure *Geophysics*, **65**, 1476-1488.

Hui-Ping, T, Veeramani, D., Kunigahalli, R., Russell, J.S., Tezkan, B., Goldman, M., Greinwald, S., Hördt, A., Müller, I., Neubauer, F. M. & Zacher, G., 1996. A joint application of radiomagnetotellurics and transient electromagnetics to the investigation of a waste deposit in Cologne (Germany), *Journal of Applied Geophysics*, **34**, 199-212.

Kirkendall, B. & Roberts, J., 2004. Electromagnetic Imaging of CO2 Sequestration at an Enhanced Oil Recovery Site, *Techn. Rep. No. UCRL-TR-204708, Lawrence Livermore Nat. Lab.*

Lumley, D., Adams, D., Wright, R., Markus, D. & Cole, S., 2008. Seismic monitoring of CO2 geosequestration: realistic capabilities and limitations, *SEG Techn. Prg. Exp. Abstr. 27*, 2841-2845.

Mackie, R. M., Watts, M. D. & Rodi, W., 2007. Joint 3D inversion of marine CSEM and MT data, *SEG Techn. Prg. Exp. Abstr. 26*, 574-578.

Meju, M., 1996. Joint inversion of TEM and distorted MT soundings: Some effective practical considerations, *Geophysics*, **61**, 56-65.

Newman, G. A. & Alumbaugh, D. L., 1997. Three-dimensional massively parallel electromagnetic inversion–I. Theory, *Geophys. J. Int.*, **128**, 345-354.

Newman, G. A. & Alumbaugh, D. L., 2000. Three-dimensional magnetotelluric inversion using non-linear conjugate gradients, *Geophys. J. Int.*, **140**, 410-424.

Newman, G. A. & Hoversten, G. M., 2000. Solution strategies for two- and three-dimensional electromagnetic inverse problems, *Inverse Problems*, **16**, 1357-1375.

Newman, G. A., Hoversten, G. M. & Alumbaugh, D. L., 2002. Three-dimensional magnetotulleric modeling and inversion: application to sub-salt imaging, in *Three-Dimensional Electromagnetics, Proc. Sec. Int. Symp.*, pp. 127-152, eds Zhdanov, M. S. & Wannamaker, P. E., Elsevier, Amsterdam.

Newman, G. A. & Boggs, P. T., 2004. Solution accelerators for large-scale three-dimensional electromagnetic inverse problems, *Inverse Problems*, **20**, 151-170.

Rovetta, D., Lovatini, A. & Watts, M. D., 2008. Probabilistic joint inversion of TD-CSEM, MT and DC data for hydrocarbon exploration, *SEG Techn. Prg. Exp. Abstr. 26*, 599-603.

Smith, J. T., Hoversten, G. M., Gasperikova, E. & Morrioson, H. F., 1999. Sharp boundary inversion of 2D magnetotelluric data, *Geophysical Prospecting*, **47**, 469-486.

White, D. J., 2008. Geophysical Monitoring in the IEA GHG Weyburn-Midale CO2 Monitoring and Storage Project *SEG Techn. Prg. Exp. Abstr. 27*, 2846-2849.

Zhang, Y., Abubakar, A. & Habashy, T., 2007. Model-based inversion algorithm for structural and conductivity reconstruction of marine controlled-source electromagnetic data, *23rd Annual Review of Progress Applications in Computational Electromagnetics, Expanded Abstracts*, 1269-1275.

Figures

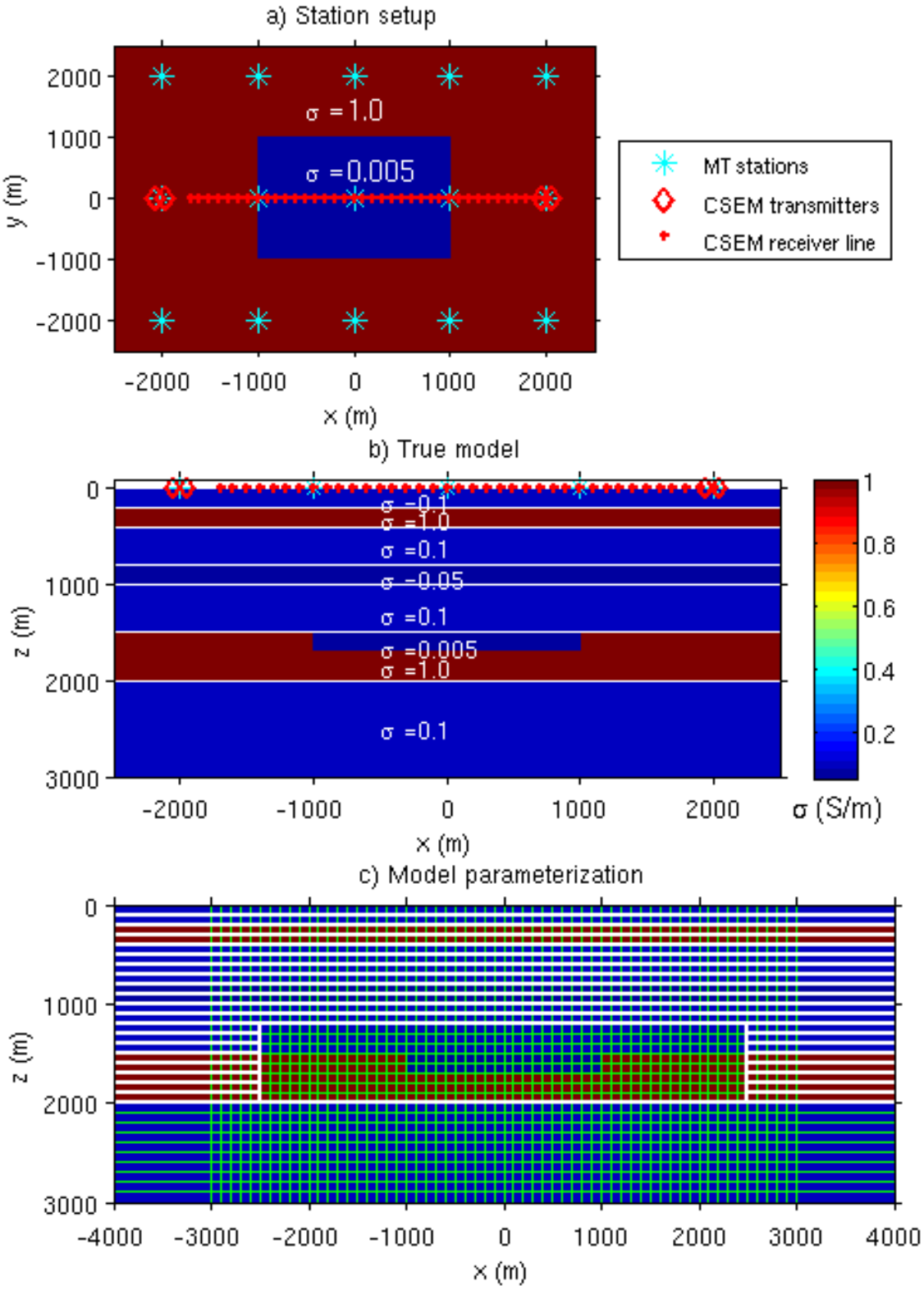

Figure 1. CO_2 sequestration monitoring study. (a) shows the station setup with a projection of the resisitive injection reservoir. (b) The true model in cross-sectional view. (c) illustrates the hybrid model parameterization. Green lines depict the model grid, white lines outline the parametric (here layers) unknowns.

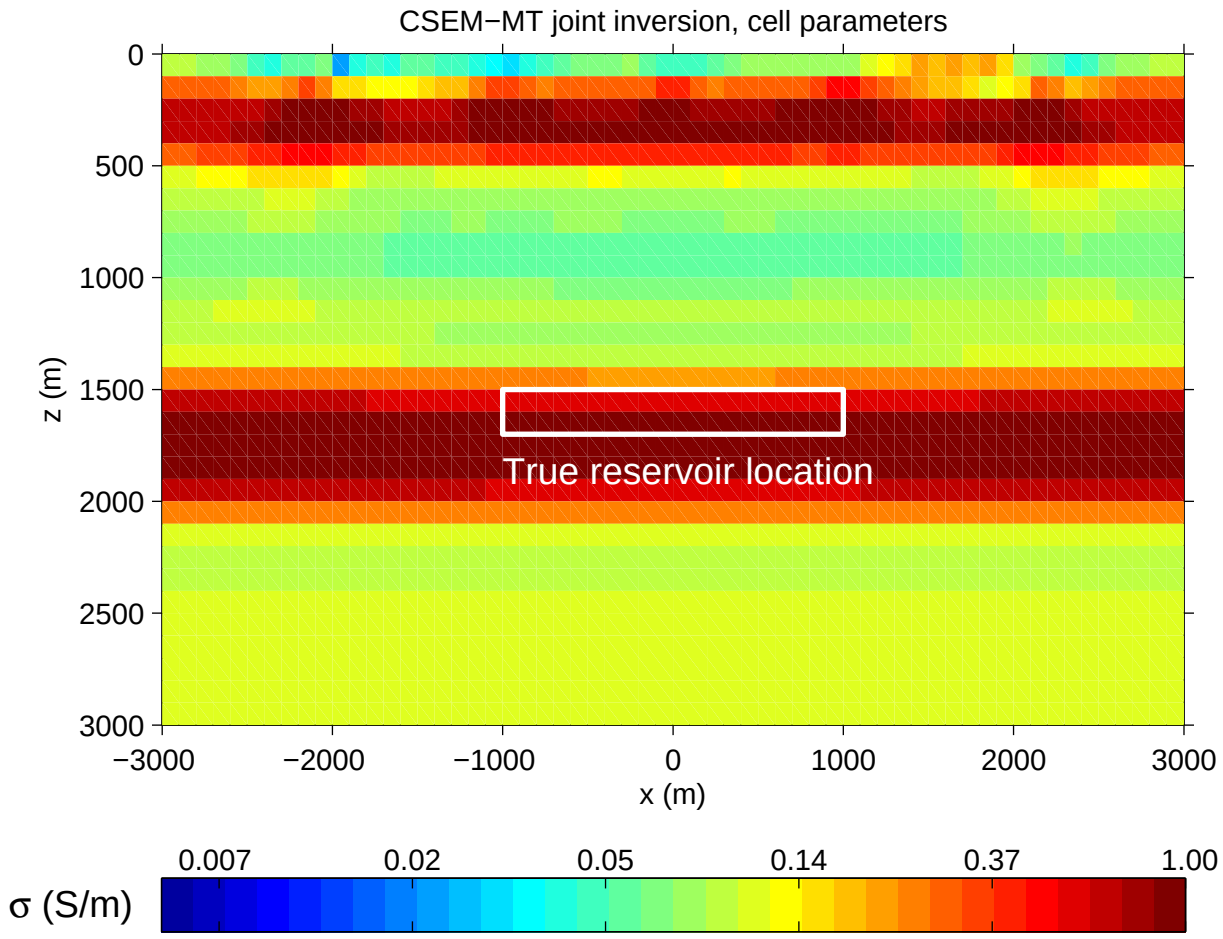

Figure 2. CO_2 sequestration monitoring study. CSEM-MT joint inversion result after 146 iterations ($RDMD = 0.5$ %) using only cell-based parameters over the whole inversion domain. The true layered background represents the starting model for this result.

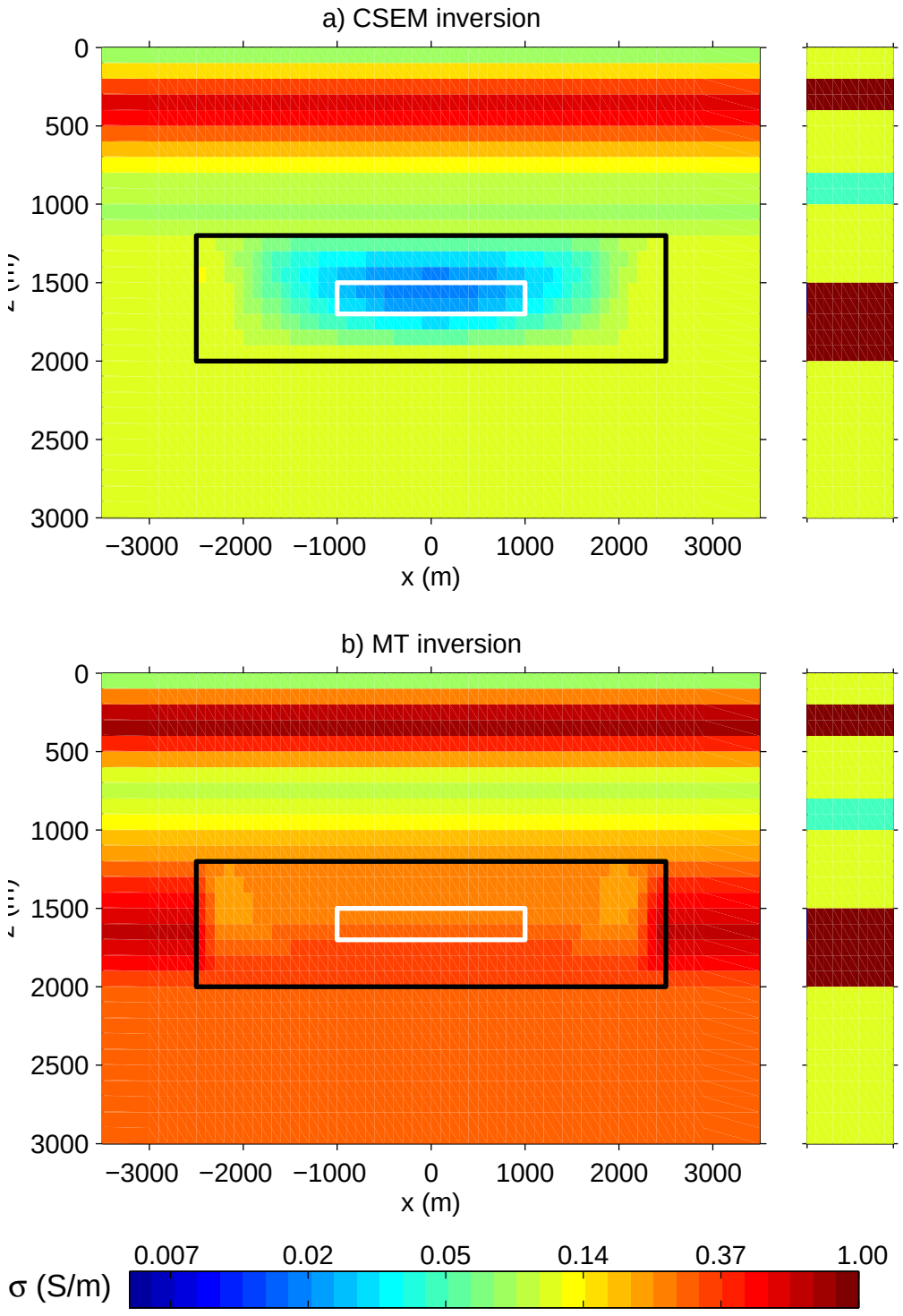

Figure 3. Standalone CSEM (a) and MT (b) inversions for the CO_2 sequestration study. The smaller figures on the right show the true layered background. The white rectangle outlines the true resistor, and the black rectangle is the volume of the cell-based parameterization.

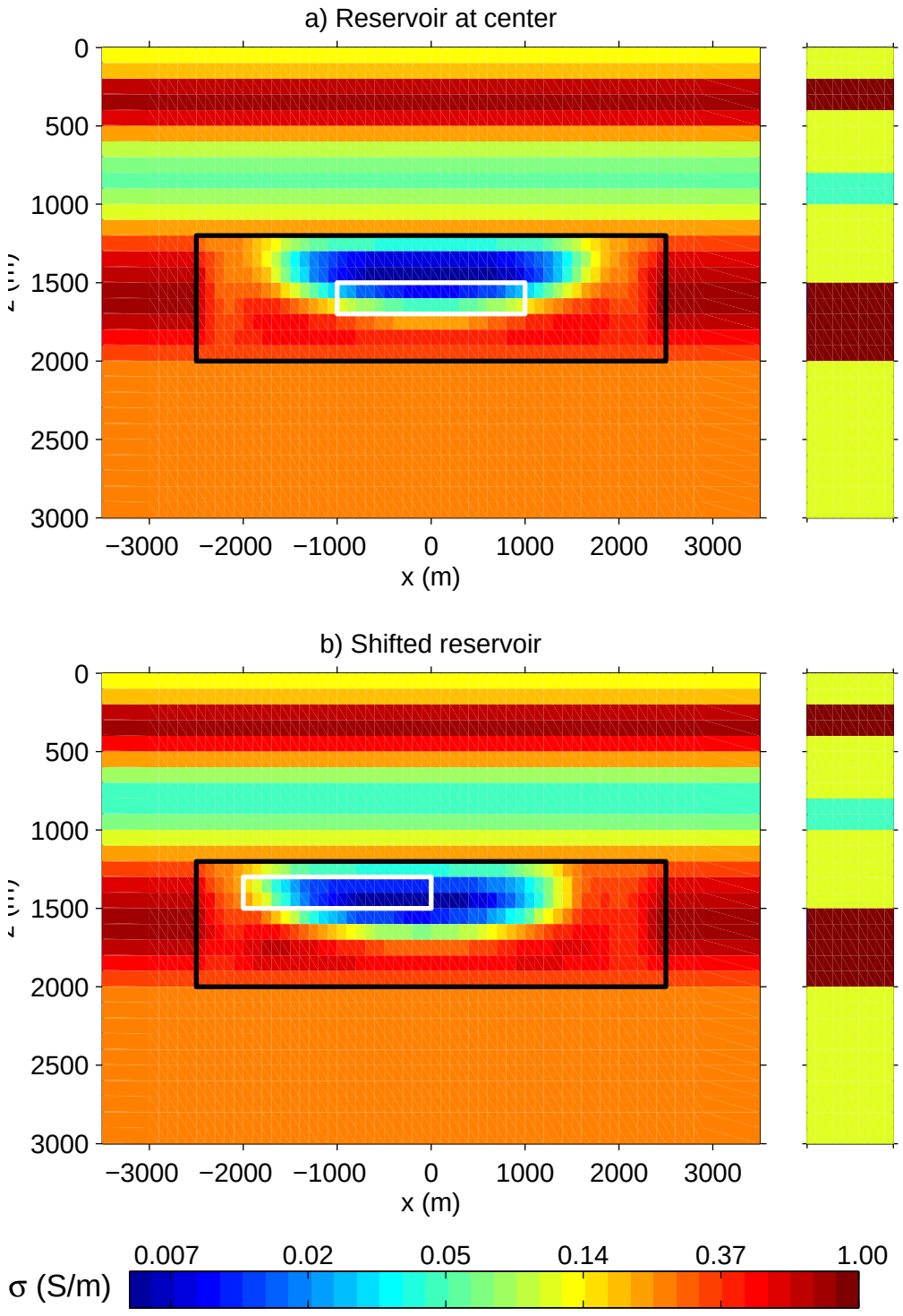

Figure 4. CSEM-MT joint inversions for a centered (a) reservoir and a shifted (b) gas reservoir.

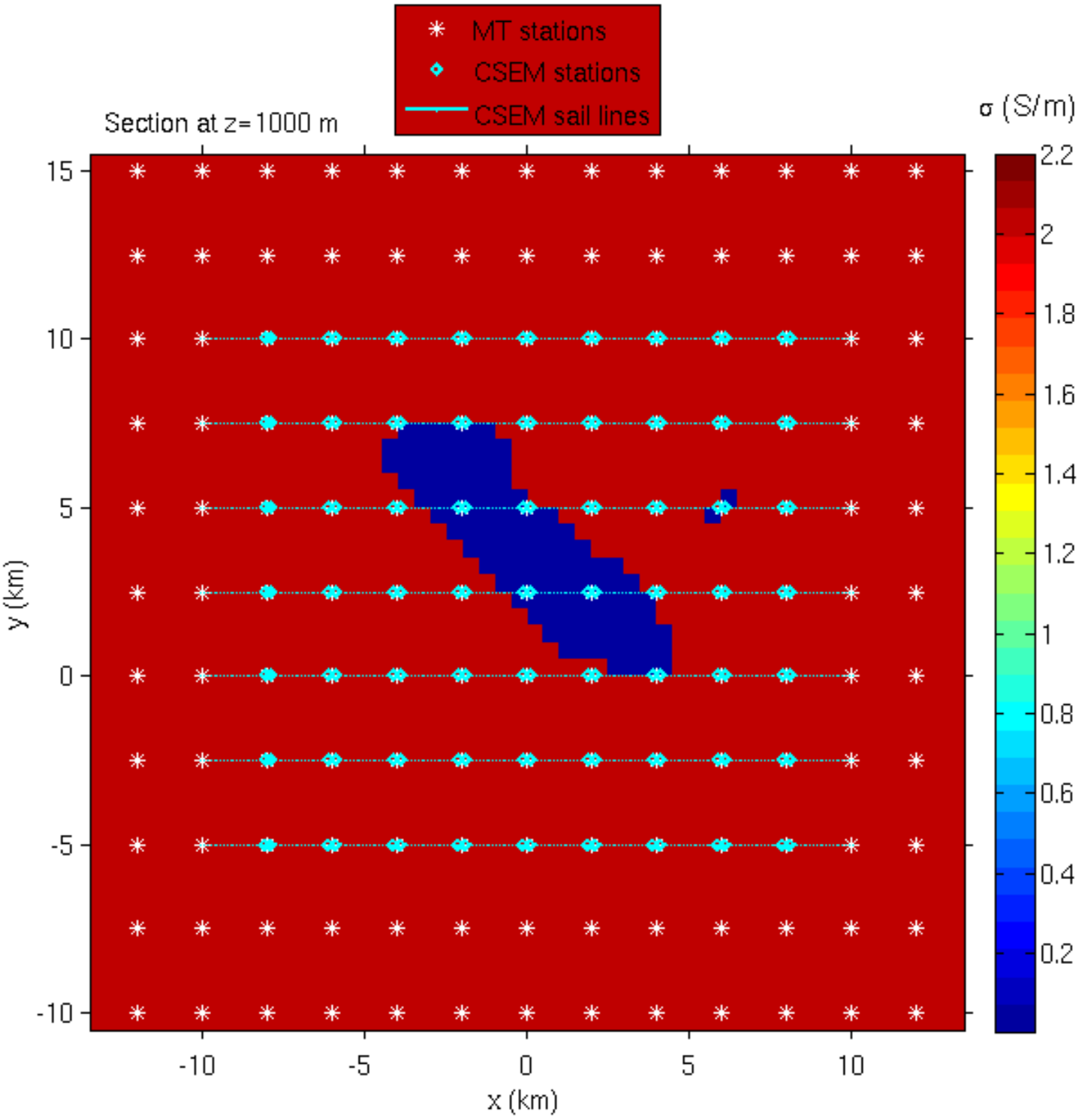

Figure 5. Marine prospecting study 1: The CSEM and MT survey layout on the seafloor ($z = 0$) is shown together with a projection of the reservoir at a depth of $z = 1$ km.

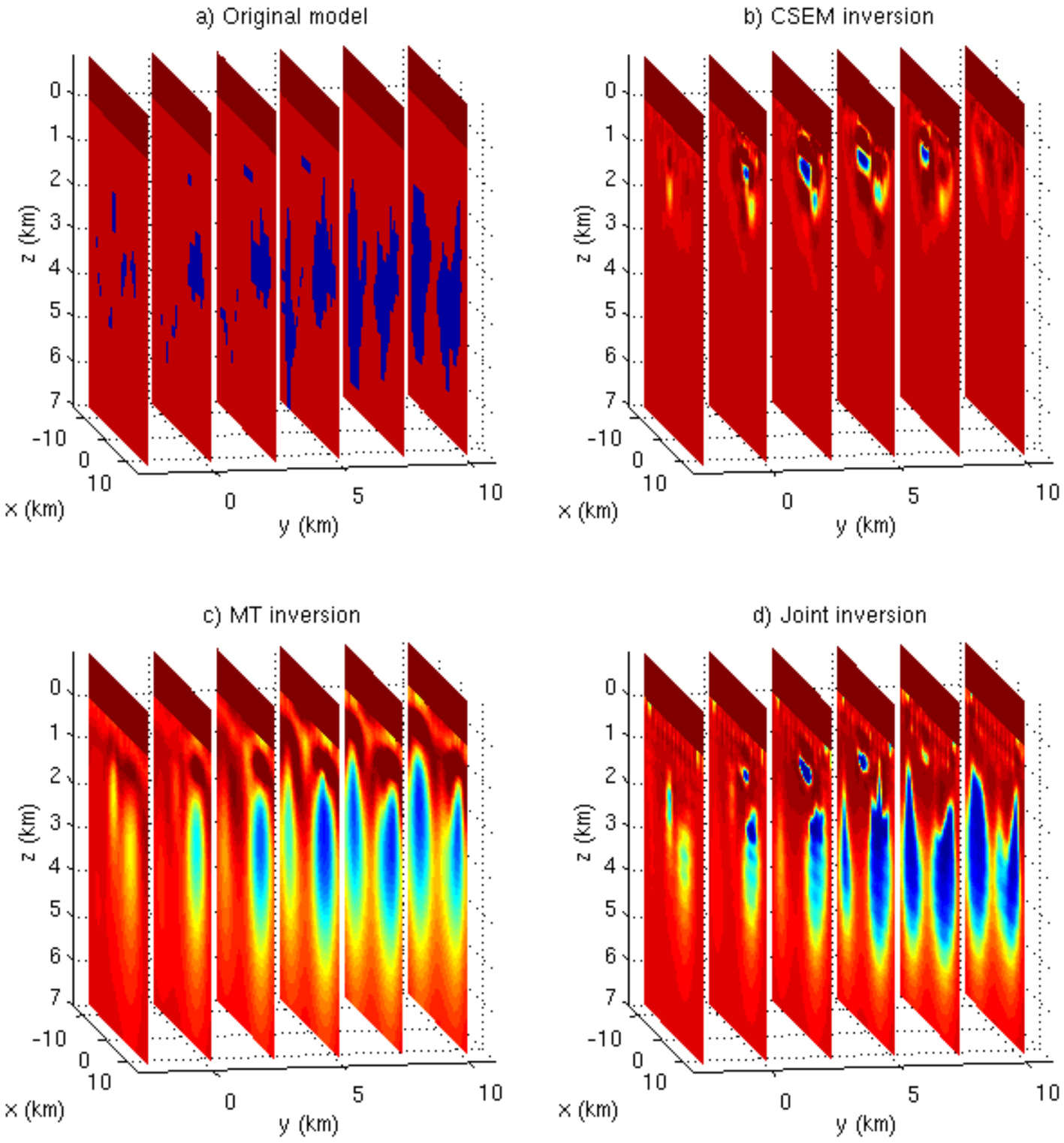

Figure 6. Marine prospecting study 1: Original model (a), CSEM inversion (b), MT inversion (c), and joint inversion (d) in a $x - z$ cross-sectional view. The color scale corresponds to Fig. 5.

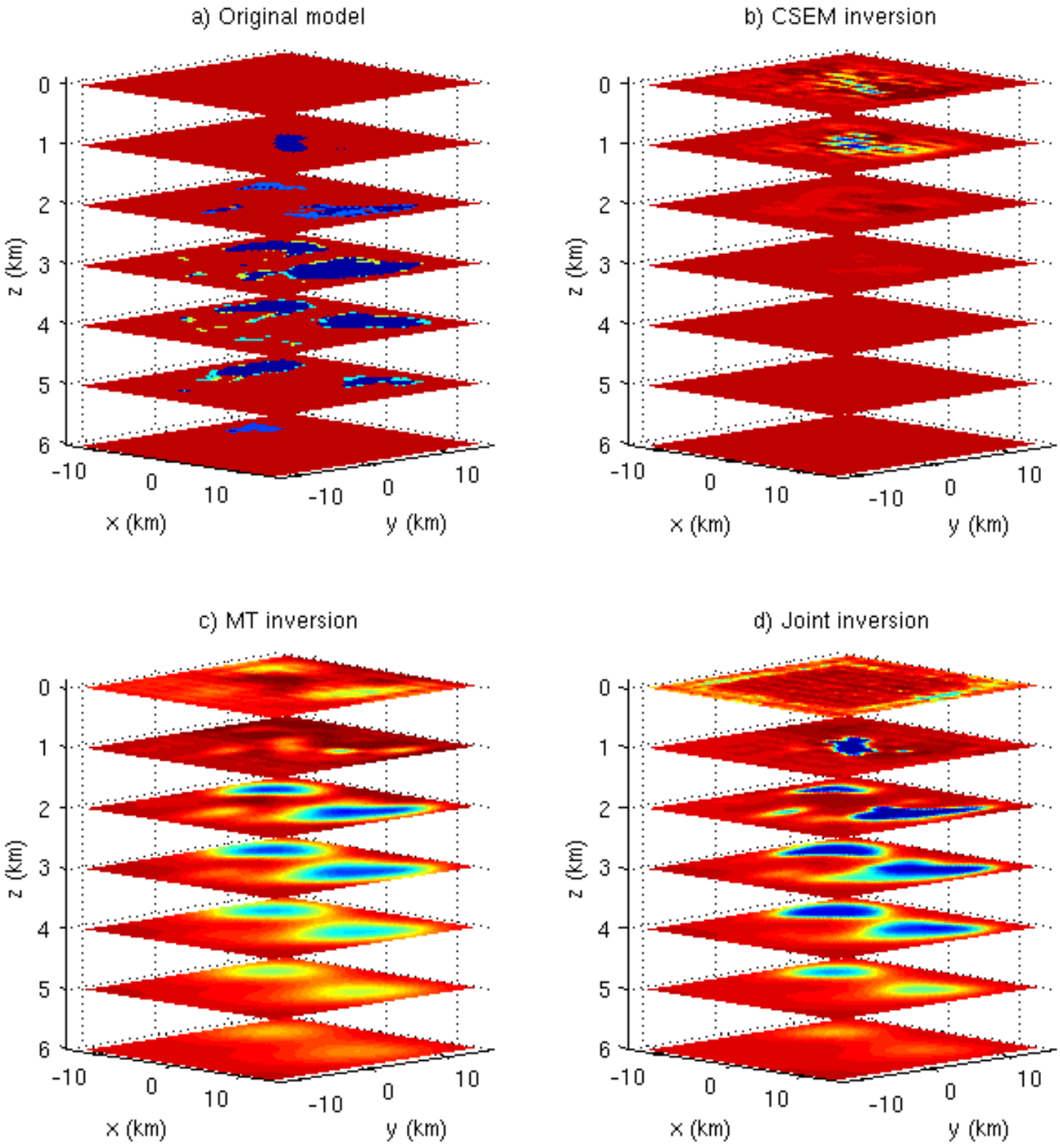

Figure 7. Marine prospecting study 1: Original model (a), CSEM inversion (b), MT inversion (c), and joint inversion (d) viewed in horizontal depth sections from 0 to 6 km. The color scale corresponds to Fig. 5

.

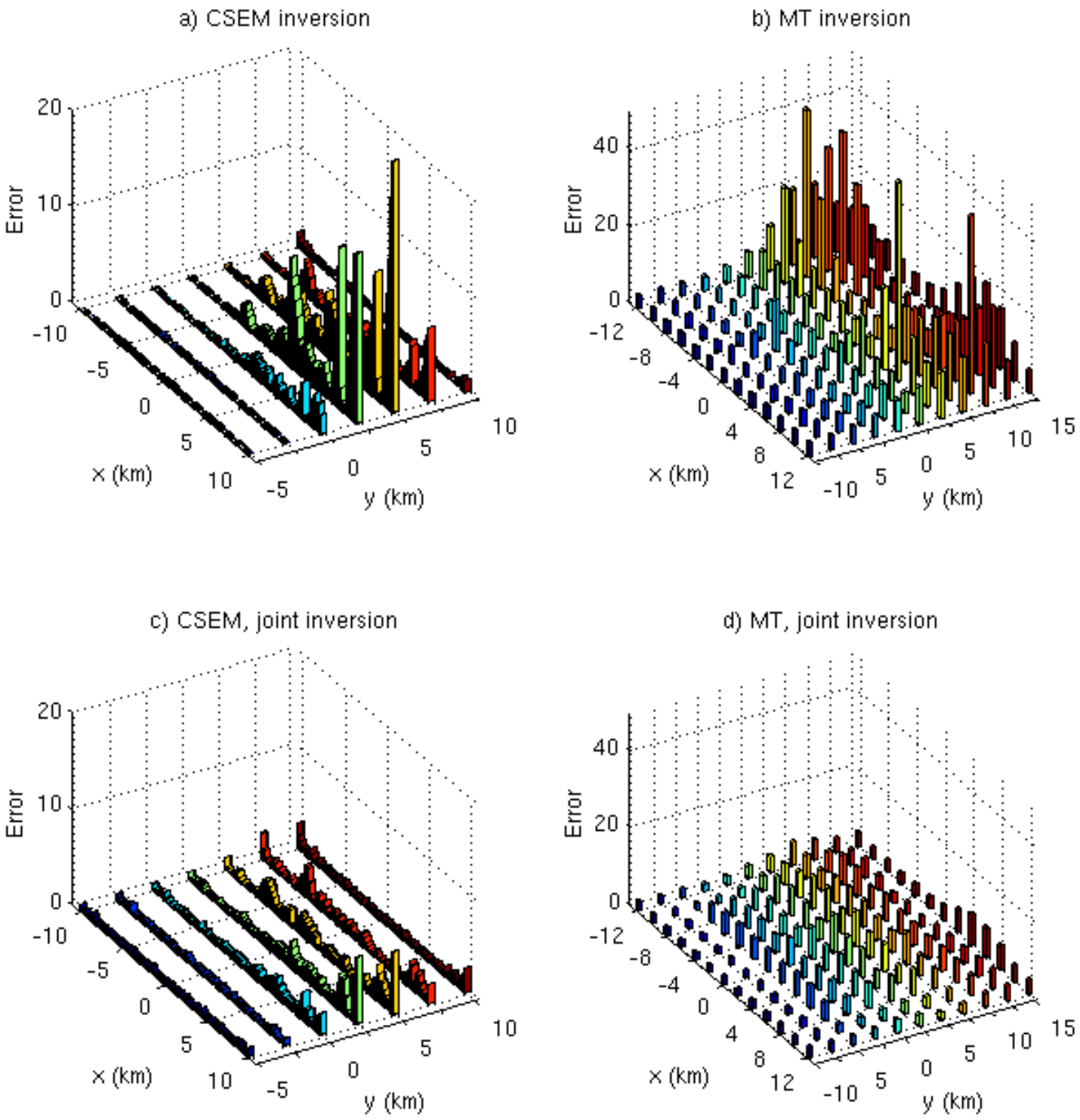

Figure 8. Marine prospecting study 1: Data fitting errors plotted along the CSEM receiver profiles and MT station profiles. (a) and (b) are produced from the standalone CSEM and MT inversions; (c) and (d) are the CSEM and MT data fits computed from the joint inversion result. Note that for a comparison, the MT data fits are both calculated using the enhanced weights (up-weighted by a factor of $f_w = 10$).

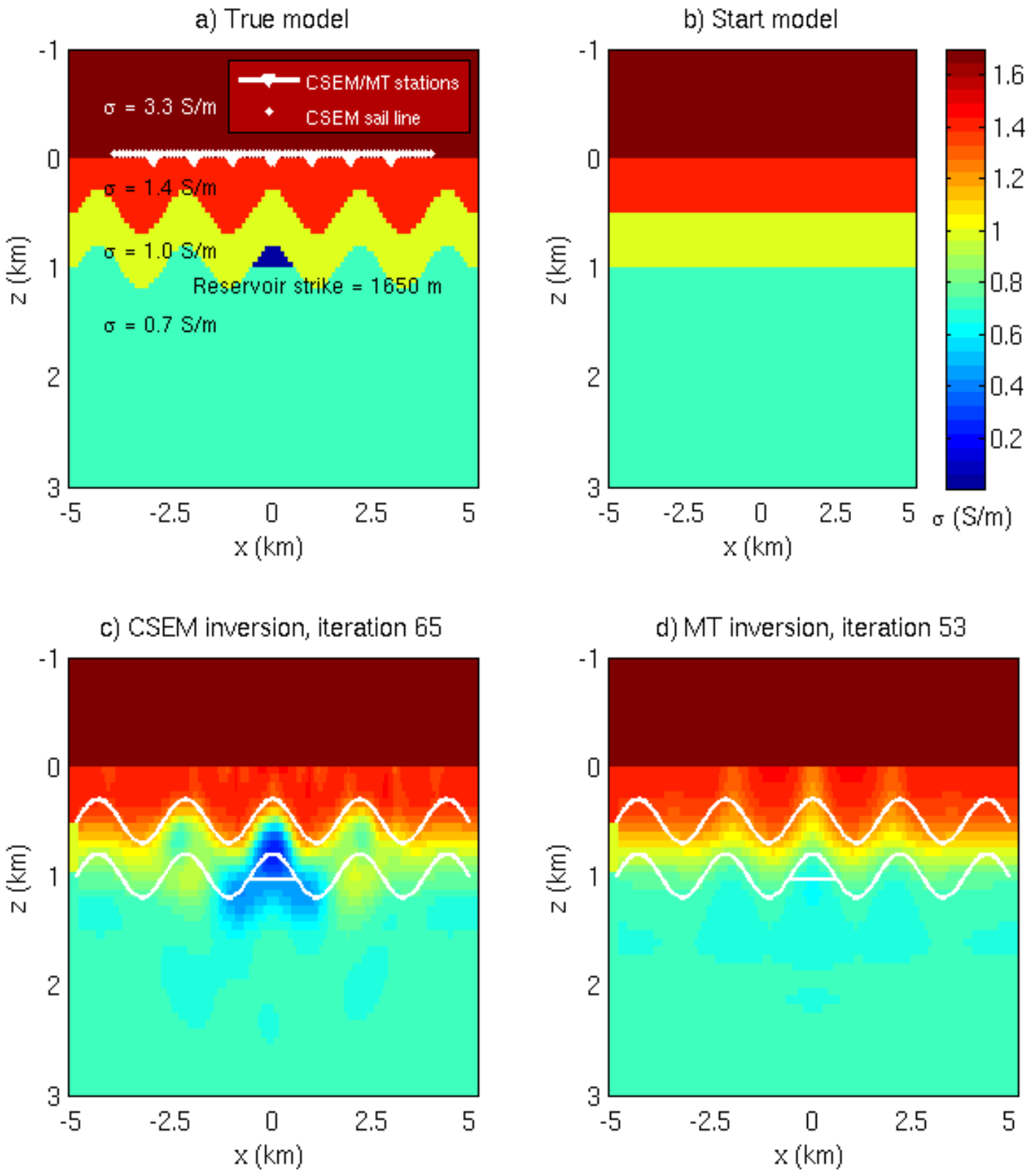

Figure 9. Marine prospecting study 2: Original model (a), starting model (b), CSEM inversion (c), and MT inversion (d) in a $x - z$ cross-sectional view.

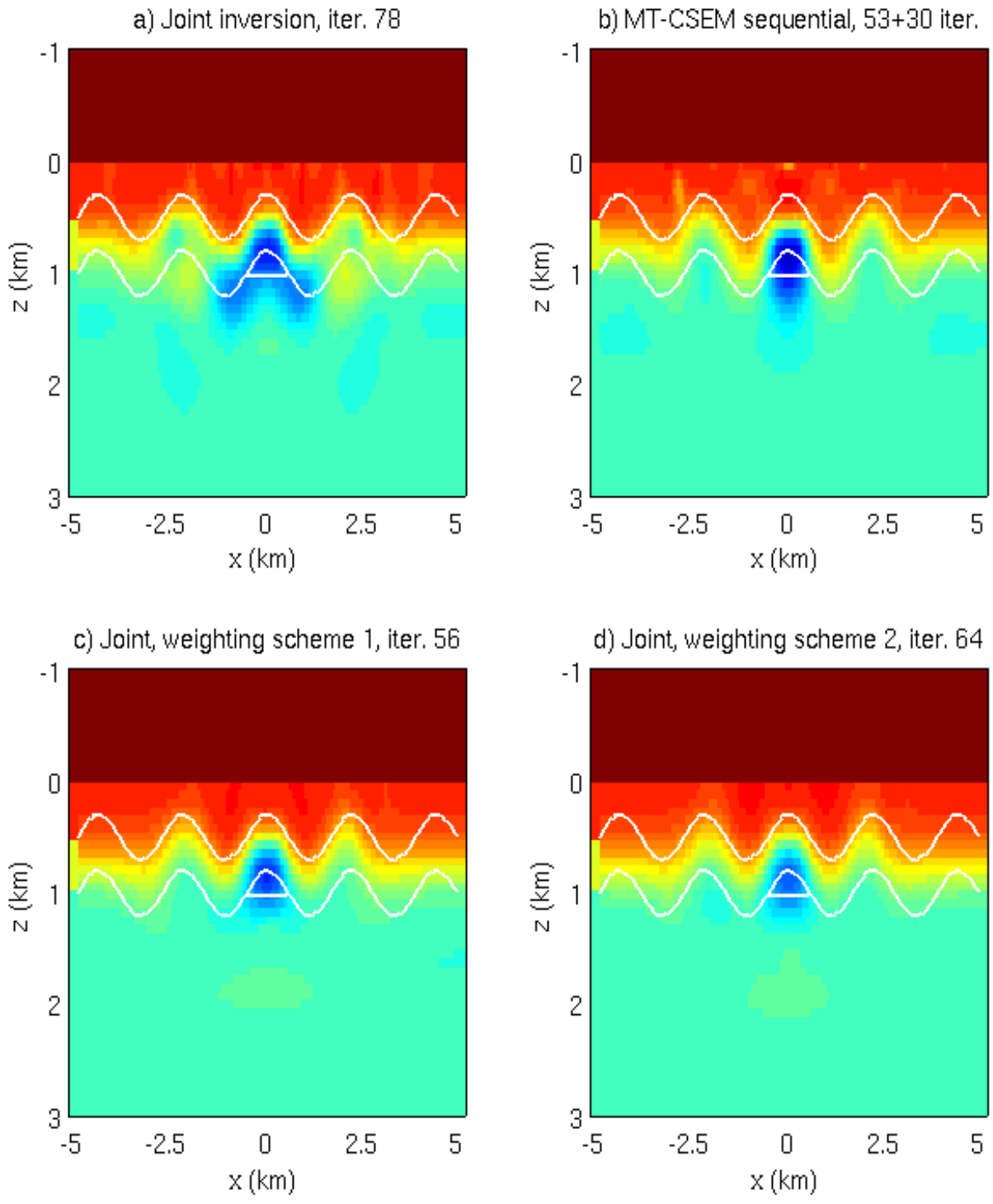

Figure 10. Marine prospecting study 2: Results (a) and (b) are produced from the original synthetic data weights, inverting the CSEM and MT data sets simultaneously and sequentially, respectively. (c) and (d) are images produced from inversions employing two different ways of estimating balanced data weights.